doi:10.1016/j.ijrobp.2011.01.046

PHYSICS CONTRIBUTION

INTERNAL FIDUCIAL MARKERS AND SUSCEPTIBILITY EFFECTS IN MRI—SIMULATION AND MEASUREMENT OF SPATIAL ACCURACY

JOAKIM H. JONSSON, M.SC.,* ANDERS GARPEBRING, M.SC.,* MAGNUS G. KARLSSON, PH.D.,*
AND TUFVE NYHOLM, PH.D.†

*Radiation Physics Section and †Section of Oncology, Department of Radiation Sciences, Umeå University, Umeå, Sweden

Background: It is well-known that magnetic resonance imaging (MRI) is preferable to computed tomography (CT) in radiotherapy target delineation. To benefit from this, there are two options available: transferring the MRI delineated target volume to the planning CT or performing the treatment planning directly on the MRI study. A precondition for excluding the CT study is the possibility to define internal structures visible on both the planning MRI and on the images used to position the patient at treatment. In prostate cancer radiotherapy, internal gold markers are commonly used, and they are visible on CT, MRI, x-ray, and portal images. The depiction of the markers in MRI are, however, dependent on their shape and orientation relative the main magnetic field because of susceptibility effects. In the present work, these effects are investigated and quantified using both simulations and phantom measurements.

Methods and Materials: Software that simulated the magnetic field distortions around user defined geometries of variable susceptibilities was constructed. These magnetic field perturbation maps were then reconstructed to images that were evaluated. The simulation software was validated through phantom measurements of four commercially available gold markers of different shapes and one in-house gold marker.

Results: Both simulations and phantom measurements revealed small position deviations of the imaged marker positions relative the actual marker positions (<1 mm).

Conclusion: Cylindrical gold markers can be used as internal fiducial markers in MRI.   © 2012 Elsevier Inc.

Fiducial markers, Gold, Magnetic resonance, Radiotherapy, Susceptibility.

INTRODUCTION

Successful external radiotherapy of prostate cancer relies on high spatial accuracy both in delineation of the target volume and in the positioning of the patient at treatment. Since the introduction of three-dimensional conformal radiation therapy (3D-CRT), computed tomography (CT) has been the standard imaging modality for the delineation of the target volume, planning of the treatment, and as reference for image-guided patient positioning at treatment. However, in recent years, the problems with CT-based target delineation have been highlighted. In a recent review, Njeh points out that image-guided radiotherapy (IGRT) improves the treatment precision but does not improve the accuracy of the treatment [1]. The accuracy of the treatment relies on the accuracy of the target volume definition, the reference image used to position the patient, and on the accuracy in the relation between the two. Gao *et al.* used the Visible Human Project® man to compare prostate delineations based on CT images of the frozen cadaver with expert delineations of the prostate gland on anatomical photos [2]. The results revealed a relatively low intraobserver variation, but also a systematic, clinically significant displacement of the delineation in the anterior direction. On average, the delineations on CT overestimated the volume of the prostate with 30%, which is comparable to the observed differences between prostates delineated on magnetic resonance imaging (MRI) compared with CT. Rasch *et al.* found that physicians on average delineated 40% larger volumes on CT compared with MRI [3]. Villeirs *et al.* found a smaller reduction of the delineated volume using MRI (6%) [4]. They did, however, observe a significantly reduced interobserver variation for MRI delineations compared with CT. Debois *et al.* noted a significant reduction of the prostate volume when delineated on transversal or coronal MRI images compared with CT, and did also observe a reduced intraobserver variation [5]. Interestingly, the results from Gao *et al.* suggest that CT-based delineations of the prostate tends to underestimate the prostate extension in the posterior direction. There are also indications that there is a systematic difference

---

Reprint requests to: Joakim H. Jonsson, M.Sc., Radiation Physics Section, Department of Radiation Sciences, Umeå University, 90187 Umeå, Sweden. Tel: (+46) 907852296; Fax: (+46) 907851588; E-mail: joakim.jonsson@radfys.umu.se

between the delineation on MRI and CT in this direction, where MRI delineations tend to cover larger volumes in the posterior direction (4, 6). This needs to be verified in further studies because other groups have presented different results (3).

The overall conclusion when reviewing the literature is that MRI is preferred to CT for prostate delineations. This has also been shown explicitly by Khoo *et al.*, who scored physicians impressions of MRI and CT images for delineation of structures related to prostate treatment (7).

There are two ways to take advantage of the superior soft-tissue contrast of MRI; either to register MRI to CT images and use this registration to transfer the segmented volume from the MRI images to the CT (5) or to fully exclude the CT from the workflow and use the MRI as basis for delineation, treatment planning, and as reference for patient setup (8–10) . The first alternative relies on accurate registration of the CT and MRIs. This is a difficult task because the prostate position relative the stable structures in the pelvic region may be different in the CT and MRI examination. To avoid registrations, the treatment planning can be performed directly on the MRIs, which reduces the systematic errors connected to the treatment (11). It has been shown in several publications that it is possible to achieve adequate dose calculation accuracy when using bulk density assignments on the MRIs (8–10, 12, 13). At present, this technique requires manual contouring to define electron density maps on the MRIs, which is time consuming and not routine. Many radiotherapy departments use CT for dose calculations and MRI for target delineation. Therefore, the exclusion of CT from the radiotherapy workflow reduces both the imaging time for each patient and the data handling at the radiotherapy department.

A precondition for an MRI-based workflow is the possibility to define internal structures that are visible both on the treatment planning MRI study and on images used to position the patient at treatment. One alternative is to use MRI in direct connection with each treatment and take advantage of the superior soft-tissue contrast of MRI also in the positioning procedure (11). Another alternative is to use the commonly employed technique with radioblique fiducial makers implanted directly into the prostate gland. These markers are visible on all commonly used x-ray systems for patient positioning, and can also be made clearly visible on magnetic resonance images (6). The visualization of the markers and their apparent positions in the images do, however, depend on their shape and orientation relative the main magnetic field (14).

In the present study, we investigate how the apparent position of the markers in MRIs correspond with their real position. We use simulation software to calculate the distortion of the static magnetic field B_0 around a gold marker with variable dimensions and how this distortion is visualized in an image. The simulations are validated through an experimental part where markers from different vendors are imaged in a phantom, with varying frequency encoding directions, band width, marker orientation, and sequence parameters.
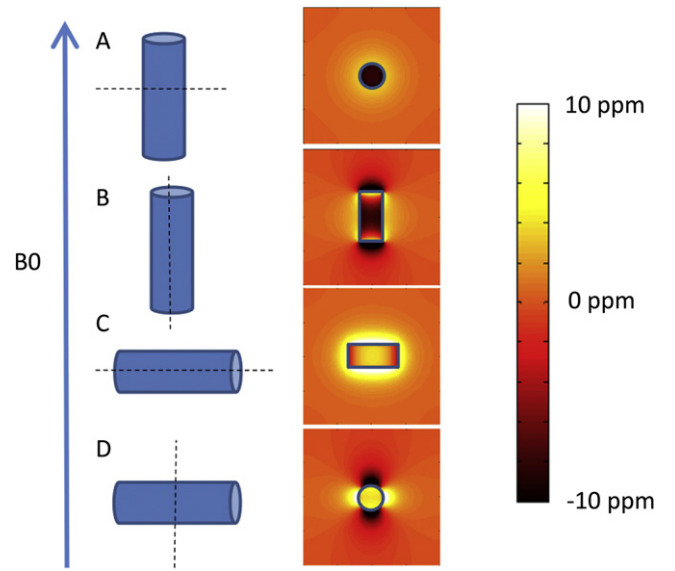

Fig. 1. Simulations of the magnetic field distortion in the different imaging geometries around cylindrical gold markers. The markers in the simulation have a radius of 0.8 mm and a length of 3 mm.

METHODS AND MATERIALS

The methodology in the present work was to simulate the marker-induced perturbations of the main magnetic field and the resulting image artifact and determine how the position of this artifact is related to the real marker position as a function of various fundamental sequence and marker properties. To validate the simulation procedure, we used phantom measurements.

Internal gold markers used as landmarks for external radiotherapy are typically shaped as solid cylinders with a length between 3 and 5 mm and the diameter of 0.9–1.6 mm. The typical material is 24-carat gold, which has a magnetic susceptibility that differs 25 ppm from water ($\chi_{Gold} = -34 \cdot 10^{-6}$, $\chi_{Water} = -9 \cdot 10^{-6}$).

The perturbation of the magnetic field is not limited to the marker but also affects a small volume around the marker. This extended perturbation is dependent on the orientation of the marker relative the main magnetic field (14).

Simulation

To simulate the image distortion caused by a material placed in a magnetic field $\mathbf{B}_0 = B_0\hat{\mathbf{z}}$, we investigate the magnetostatic macroscopic Maxwell equations. In MRI, the polarizing field is much greater than the magnetization, such that the assumption

$$\mu_0 M_z = \chi B_0 \qquad (1)$$

where μ_0 is the vacuum permeability, M_z is the magnetization, and χ is the susceptibility of the material is valid. From previous work by de Rochefort *et al.* (15), it is known that the measurable shift of **B** after Fourier transformation is

$$\mathbf{b}_{local} = \mu_0 \left(\frac{1}{3}\mathbf{m} - \frac{\mathbf{k}}{k^2}\mathbf{k}\cdot\mathbf{m} \right), \qquad (2)$$

where **k** is the position in the Fourier domain, **m** is the Fourier transform of the magnetization, and $\mathbf{b}_{local}$ is the Fourier transform of the local magnetic shifts. Taking the inverse Fourier transform of Eq. 2, we have the perturbation map $P(x,y,z)$, which describes the distortion of the local magnetic field, including susceptibility effects.

Table 1. Information concerning the markers included in the phantom study

	Vendor	Type	Cross–section	Shape	Length
1	Civco	24 h Gold	∅1.6 mm	Circular	3 mm
2	In-house	18 h Gold	∅1.5 mm	Circular	3 mm
3	Civco	24 h Gold	∅1.2 mm	Circular	3 mm
4	Beampoint	24 h Gold	∅1.0 mm	Star shaped	3 mm
5	Visicoil	24 h Gold	∅0.75 mm	Spiral shaped	3 mm

The perturbation map $P(x,y,z)$ for the main magnetic field can be directly recalculated into a displacement map $\vec{\mathbf{D}}(x, y, z)$ defined as

$$\vec{\mathbf{D}}(x, y, z) = \gamma P(x,y,z) \cdot \left[\frac{\hat{\mathbf{x}}(VS_x)}{BW_x}, \frac{\hat{\mathbf{y}}(VS_y)}{BW_y}, \frac{\hat{\mathbf{z}}(VS_z)}{BW_z} \right], \quad (3)$$

where VS represents the voxel size, BW the bandwidth per voxel (Hz/VS) in the different directions, and γ is the resonance frequency. In phase-encoding directions, BW is set to $-\infty$.

The signal from a given position (x,y,z) in the scanner hence contributes to the image in the position

$$\left[x_{image}, y_{image}, z_{image} \right] = [x, y, z] + \vec{\mathbf{D}}(x, y, z) \quad (4)$$

.

In the simulations, the signal contribution was assumed to be homogeneous in matter surrounding the markers, and zero within the marker. This assumption corresponds to a spin echo-based sequence where the dephasing of the spins plays a minor role. The field distortions of different marker orientations are shown in Fig. 1.

Measurements for validation of simulation method

All experiments were conducted using a 1.5T Siemens Espree (Siemens, Erlangen, Germany), with a four-channel standard head coil.
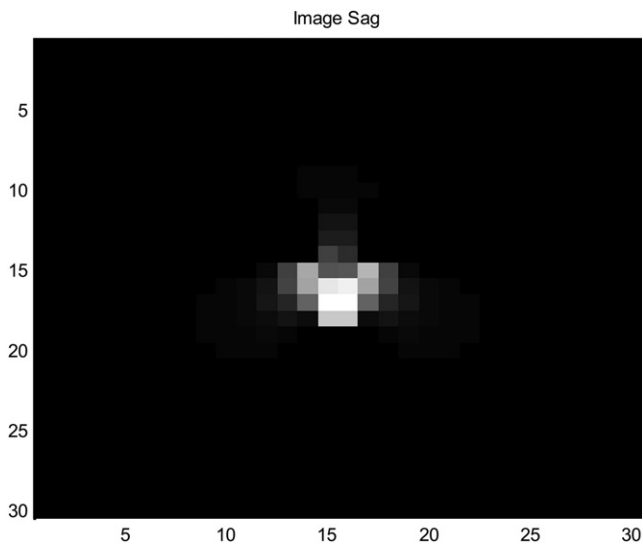

Fig. 2. The thresholded and inverted evaluation volume used for center of mass calculations. The operations were performed on a simulation gold marker with a diameter of 1.6 mm and a length of 3 mm. Simulation was performed with sagittal slices, and the marker was positioned perpendicular the main magnetic field (geometry D). $BW_y = 70$ Hz/VS$_x$, $BW_z = 1,200$ Hz/VS$_z$; $VS = (0.52, 0.52, 1.1)$ mm, where BW indicates bandwidth.
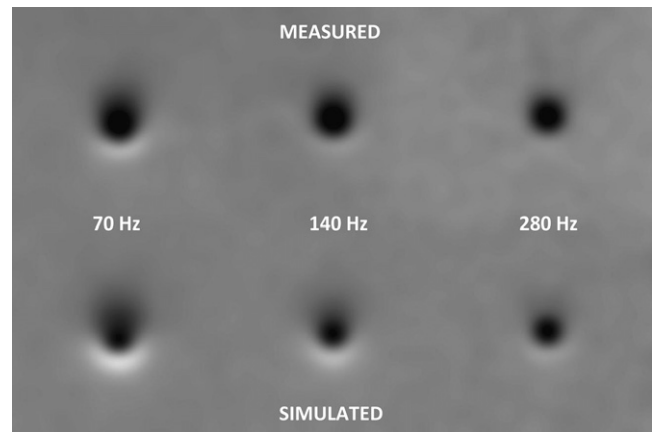

Fig. 3. Measurement and simulation of a gold marker with a diameter of 1.6 mm and a length of 3 mm. Imaging and simulation was performed with transversal slices, and the marker was positioned along the main magnetic field (geometry A) with frequency encoding in the y direction (up-down in the image). $BW_z = 1,200$ Hz/VS$_z$, $VS = (0.52, 0.52, 1.1)$ mm. The images were low-pass-filtered to eliminate pixel edges and Gaussian noise was added to simulations to replicate the measurements. BW = bandwidth.

Gold markers from different vendors and of different dimensions (Table 1) were positioned in a homogenous gelatin phantom. The amount of gelatin was adjusted to keep the resonance frequency of the phantom equal to that of water. The water equivalence was validated by imaging a thin layer of water on the gelatin with frequency-encoding perpendicular to the water layer. For the phantom used, there was no visible interface between the two materials.

The phantom was scanned with the markers positioned with the central axis along or perpendicular to the main magnetic field B_0. Two sequences were used: 1) 3D Turbo Spin Echo SPACE sequence (Siemens) with varying flip angle on the refocusing pulses and 2) two-dimensional (2D) Turbo Spin Echo sequence. The 3D sequence was run with the following settings: repetition time 3,000 ms, echo time 24 ms, matrix size 128 × 128, pixel size 0.93 × 0.93 mm^2, slice thickness 1 mm, and bandwidth 70, 140,
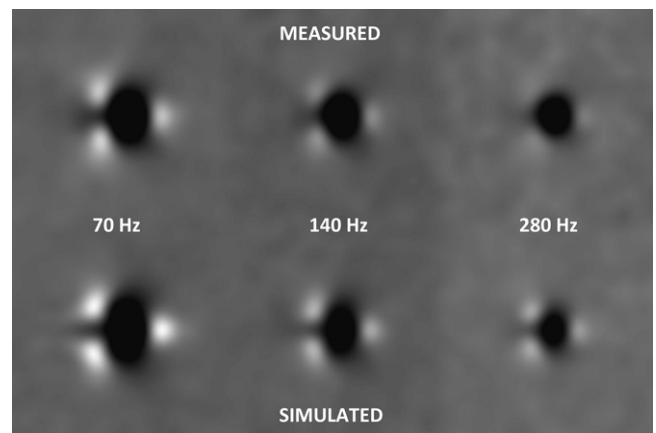

Fig. 4. Measurement and simulation of a gold marker with a diameter of 1.6 mm and a length of 3 mm. Imaging and simulation was performed with sagittal slices, and the marker was positioned perpendicular to the main magnetic field (geometry D) with frequency encoding in the y direction (left-right in the image). $BW_z = 1,200$ Hz/VS$_z$, $VS = (1.1, 0.52, 0.52)$ mm. The images were low pass filtered to eliminate pixel edges and Gaussian noise was added to simulations to replicate the measurements. BW = bandwidth.
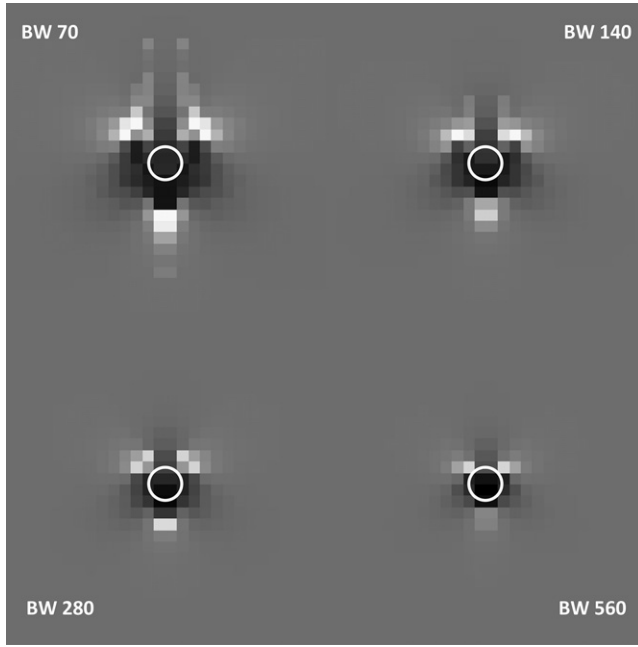
Fig. 5. Marker positions for different bandwidths (BW). The marker placement is shown by the circle overlay on top of the corresponding simulated image. Simulation performed with $BW_z = 1,200$ Hz/VS$_z$, VS = (0.52, 0.52, 1.1) mm and in-plane bandwidth 70 Hz/pixel, 140 Hz/pixel, 280 Hz/pixel, and 540 Hz/pixel.

and 280 Hz/pixel. The 2D sequences were acquired both with the same spatial settings as the 3D sequence to enable comparison, and with higher spatial resolution according to: repetition time 3,000 ms, echo time 18 ms, matrix size 192 × 192, pixel size 0.52 × 0.52 mm^2, slice thickness 1 mm, and bandwidth 70, 140, and 280 Hz/pixel.

Because the deviations of the imaged positions from the actual marker positions are very small, there is no method for sufficiently accurate absolute measurements. Instead we recorded the apparent marker position of a fiducial in two different sequences (*e.g.*, after switching phase-encoding directions). The difference in these positions corresponds to the marker deviation, because inplane susceptibility errors are only visible in the frequency encoding direction.
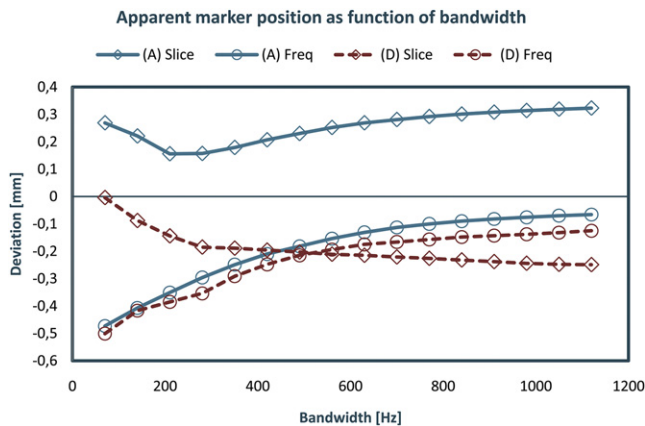

Fig. 6. Plots showing the apparent marker position deviation for different bandwidths (BW) in geometry A and D, using a two-dimensional sequence with frequency encoding in the y direction. $BW_z = 1,200$ Hz/VS$_z$, VS = (0.52, 0.52, 1.1) mm.
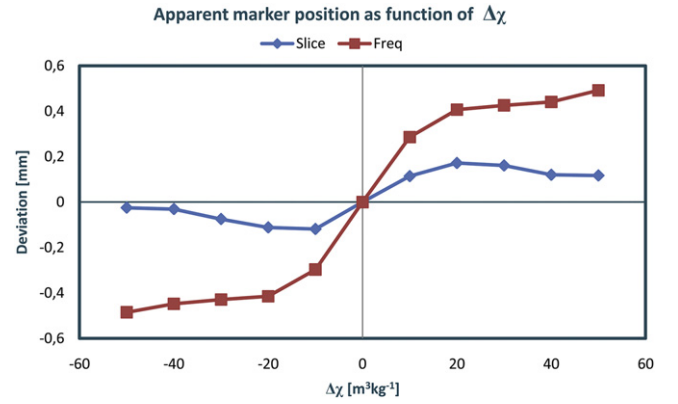

Fig. 7. Plot of the apparent marker position as a function of marker susceptibility. Simulation of geometry A using a two-dimensional sequence with frequency encoding in the y direction with inplane bandwidth 140 Hz/pixel, $BW_z = 1,200$ Hz/VS$_z$ and VS = (0.52, 0.52, 1.1) mm. BW = bandwidth.

Determination of apparent marker position

To determine the apparent position of the marker in the phantom images, we developed software that localized the center of mass of the signal loss caused by the marker. By clicking a point within the area of marker signal loss in three views (sagittal, coronal, and transverse), the software extracted a small evaluation volume around the marker. This volume was interpolated cubically to four times its original size, eliminating discontinuities at the voxel edges. Using thresholding, the lowest intensities were selected, on which the image was inverted (Fig. 2) and the center of mass calculated. In the simulations, the apparent position was determined in a similar manner, without the need to manually select the marker position as a starting point.

RESULTS

Validation of simulation method

Figures 3 and 4 display comparisons of actual phantom images and their corresponding simulations. Both measurements and simulations show a reduction in artifact size with increased bandwidth. The artifact is symmetrical
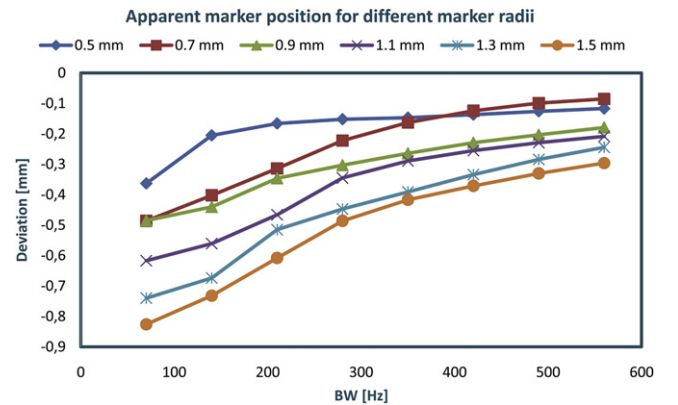

Fig. 8. Plot of the apparent marker position as a function of bandwidth for different marker radii. Simulation of geometry A using a two-dimensional sequence with frequency encoding in the y direction, $BW_z = 1200$ Hz/VS$_z$ and VS = (0.52, 0.52, 1.1) mm. BW = bandwidth.
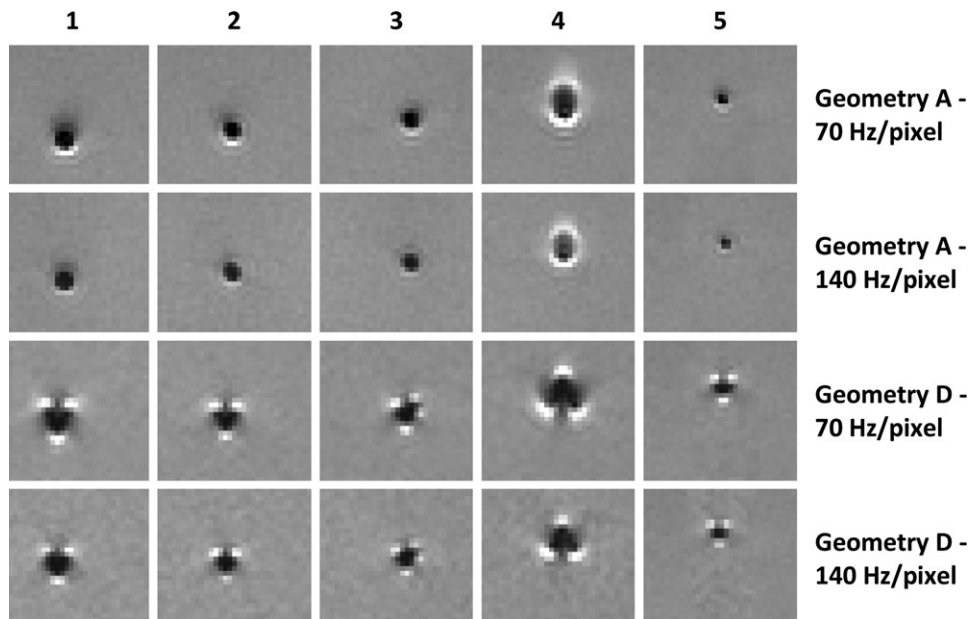
Fig. 9. Example of images of the five different markers (indicated by the number in the top) for different orientations and bandwidth (indicated to the right).

in the phase encoding direction. As can be seen, the visual differences between the simulated and measured images were small.

Simulations

Apparent marker position and bandwidth. We did not observe any significant displacements (maximum, 0.5 mm) of the apparent marker position when studying the range from 70 to 1120 Hz/pixel. The artifacts were significantly less pronounced in the images with higher bandwidth. Figure 5 show the simulated images for different bandwidths and Fig. 6 displays a plot of the calculated marker positions for different bandwidths.

Apparent marker position and susceptibility. The susceptibility effect causes small deviations in apparent marker position (maximum, 0.4 mm) in the investigated range of $\Delta\chi$ from -50 m^3/kg^{-1} to 50 m^3/kg^{-1} (Fig. 7.). At $\Delta\chi = 0$, the apparent marker deviation from real position is of course zero. When $\Delta\chi$ changes sign, the artifact pattern is mirrored and the apparent marker deviation also changes sign.

Apparent marker position and marker radius. Marker size affects the apparent marker position. A larger marker ra-

dius will produce a larger deviation of the apparent marker position compared to the actual position (Fig. 8). A very small marker will, however, be hard to detect on a low-resolution MRI scan. The maximum deviation at 70 Hz for the largest simulated marker ($r = 1.5$ mm) was 0.8 mm. Corresponding value for the standard marker $r = 0.8$ mm was 0.5 mm.

Measurements

Figure 9 shows examples of the images of the markers. It is obvious that the depiction of the markers is dependent on the orientation of the marker relative the main magnetic field and that an increase in bandwidth decreases the size of the artifact. It can also be seen that both the shape and size of the markers affect the size of the artifact. The Beampoint marker (marker 4) produced the largest artifact despite the small radius. Also note that the artifact pattern is mirrored compared with the other markers.

Table 2. The change in apparent marker position when increasing the bandwidth from 70 to 280 Hz/pixel

Sequence	Geometry	Mean deviation (standard deviation)		
		X (mm)	Y (mm)	Z (mm)
2D	A*	0.0 (0.04)	−0.30 (0.20)	−0.14 (0.22)
2D	C†	0.01 (0.14)	0.04 (0.08)	0.02 (0.35)
2D	D*	−0.14 (0.12)	−0.10 (0.12)	−0.02 (0.08)

Mean deviations for the five markers are presented together with the standard deviation.
* Slice-direction along z.
† Slice direction along x.

Table 3. The change in apparent marker position with swapped frequency and phase encoding directions for the 2D and 3D sequence

Sequence	Geometry	Mean deviation (standard deviation)		
		X (mm)	Y (mm)	Z (mm)
2D	A*	−0.15 (0.28)	−0.11 (0.26)	0.12 (0.27)
2D	C†	0.08 (0.13)	−0.14 (0.19)	−0.10 (0.28)
3D	A*	−0.09 (0.12)	−0.07 (0.21)	0.14 (0.22)
3D	C†	0.08 (0.07)	−0.02 (0.29)	−0.07 (0.24)

Abbreviations: 2D = two-dimensional; 3D = three-dimensional.
Mean deviations for the five markers are presented together with the standard deviation for an individual observation.
* Slice direction along z.
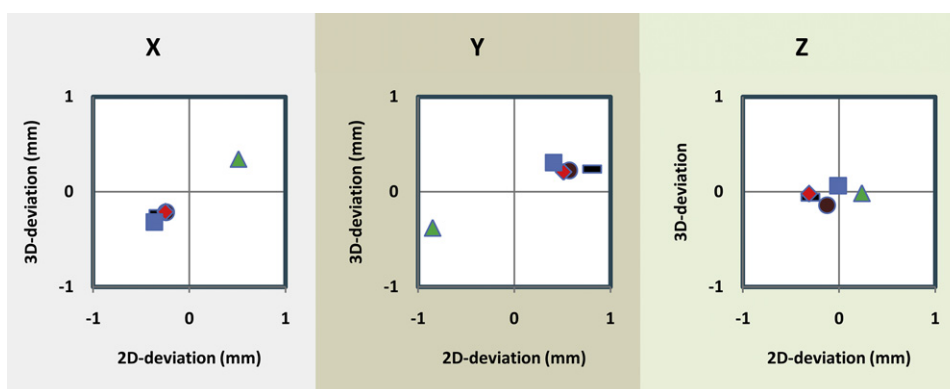† Slice-direction along x.

Fig. 10. Marker position deviations observed for geometry C when switching between phase-encoding in anteroposterior direction to head-feet direction. The x axis gives the deviation for the two-dimensional sequence and the y-axis the deviations for the three-dimensional sequence. The line represents marker 1, the circle marker 2, the rhombus marker 3, the triangle marker 4, and the square represents marker 5. See Table 1 for information regarding the markers.

Effect of bandwidth

We did not observe any significant displacements of the apparent marker position when comparing bandwidth 70 Hz/pixel and 280 Hz/pixel. Displacement data are presented in Table 2. The markers were significantly less pronounced in the images with higher bandwidth.

Effect of frequency encoding direction

Small changes in the marker positions were noticed when switching the frequency and phase encoding directions. Table 3 shows summarized data for geometry A and C and for the 2D and 3D sequence. Interestingly, when the data are broken down for individual markers, a pattern arise, as can be seen in Fig. 10. Markers 1–3 and 5 behaves similar, whereas the visualization of marker 4 deviates from the actual marker position in the opposite direction.

DISCUSSION

In general, the observed changes of apparent marker position, in simulations as well as in experiments, were very small; in all cases <1 mm. Quantification of these small deviations is extremely difficult using just the experimental data, but performed simulations support the conclusion of small marker position deviations.

The mirrored artifact pattern exhibited by the star-shaped marker 4 in the phantom images is not a property of its shape, although one might be inclined to draw that conclusion. It is most probably a material property. The marker in question is marketed as 24-carat gold, or 99.9% pure, leaving 0.1% mass unaccounted for. It has been shown that 0.1% mass iron, or other ferromagnetic material, is sufficient to change a gold alloy from diamagnetic to paramagnetic (16). It is evident from our simulations (Fig. 8) that this would explain the effect. We recommend that the MRI-related properties should be evaluated in the quality assurance program when introducing a new type of marker.

The simulations seen in Fig. 3 and 4 have slightly more pronounced artifact patterns and somewhat smaller areas of signal loss than the corresponding measurements. This is probably because of image windowing performed in the scanner software. It may also be due to differences in $\Delta\chi$ of simulations compared with the real experiments. The gelatin may differ in susceptibility from real tissue and the gold may also be impure, causing the measurements to show less susceptibility effects than the simulations because of a smaller $\Delta\chi$. If this is the case, the simulations overestimate the apparent marker deviation.

It is evident from Fig. 5 that defining the marker center at the point of lowest intensity will be more erroneous than placing it in the center of the complete artifact pattern. If the markers are to be manually defined (*e.g.*, at patient positioning), the center of the marker should be defined at the center of the entire artifact.

CONCLUSION

Both simulations and experiments show that the apparent marker position in MRIs deviates from the actual marker position by <1 mm. Cylindrical gold markers can therefore be used as internal fiducial markers in MRI.

REFERENCES

1. Njeh CF. Tumor delineation: The weakest link in the search for accuracy in radiotherapy. *J Med Phys* 2008;33:136–140.
2. Gao Z, Wilkins D, Eapen L, *et al*. A study of prostate delineation referenced against a gold standard created from the visible human data. *Radiother Oncol* 2007;85:239–246.
3. Rasch C, Barillot I, Remeijer P, *et al*. Definition of the prostate in CT and MRI: A multi-observer study. *Int J Radiat Oncol Biol Phys* 1999;43:57–66.
4. Villeirs GM, Van Vaerenbergh K, Vakaet L, *et al*. Interobserver delineation variation using CT versus combined CT + MRI in intensity-modulated radiotherapy for prostate cancer. *Strahlenther Onkol* 2005;181:424–430.
5. Debois M, Oyen R, Maes F, *et al*. The contribution of magnetic resonance imaging to the three-dimensional treatment planning of localized prostate cancer. *Int J Radiat Oncol Biol Phys* 1999; 45:857–865.

6. Parker CC, Damyanovich A, Haycocks T, *et al*. Magnetic resonance imaging in the radiation treatment planning of localized prostate cancer using intra-prostatic fiducial markers for computed tomography co-registration. *Radiother Oncol* 2003;66:217–224.

7. Khoo VS, Padhani AR, Tanner SF, *et al*. Comparison of MRI with CT for the radiotherapy planning of prostate cancer: A feasibility study. *Br J Radiol* 1999;72:590–597.

8. Chen L, Price RA Jr., Nguyen TB, *et al*. Dosimetric evaluation of MRI-based treatment planning for prostate cancer. *Phys Med Biol* 2004;49:5157–5170.

9. Chen L, Price RA Jr., Wang L, *et al*. MRI-based treatment planning for radiotherapy: Dosimetric verification for prostate IMRT. *Int J Radiat Oncol Biol Phys* 2004;60:636–647.

10. Lee YK, Bollet M, Charles-Edwards G, *et al*. Radiotherapy treatment planning of prostate cancer using magnetic resonance imaging alone. *Radiother Oncol* 2003;66:203–216.

11. Nyholm T, Nyberg M, Karlsson MG, *et al*. Systematisation of spatial uncertainties for comparison between a MR and a CT-based radiotherapy workflow for prostate treatments. *Radiat Oncol* 2009;4:54.

12. Pasquier D, Betrouni N, Vermandel M, *et al*. MRI alone simulation for conformal radiation therapy of prostate cancer: Technical aspects. *Conf Proc IEEE Eng Med Biol Soc* 2006;1:160–163.

13. Prabhakar R, Julka PK, Ganesh T, *et al*. Feasibility of using MRI alone for 3D radiation treatment planning in brain tumors. *Jpn J Clin Oncol* 2007;37:405–411.

14. Schenck JF. The role of magnetic susceptibility in magnetic resonance imaging: MRI magnetic compatibility of the first and second kinds. *Med Phys* 1996;23:815–850.

15. de Rochefort L, Nguyen T, Brown R, *et al*. In vivo quantification of contrast agent concentration using the induced magnetic field for time-resolved arterial input function measurement with MRI. *Med Phys* 2008;35:5328–5339.

16. Silvestri Z, Davis RS, Geneves G, *et al*. Volume magnetic susceptibility of gold-platinum alloys: Possible materials to make mass standards for the watt balance experiment. *Metrologia* 2003;40:172–176.